Real-time 3D single-molecule localization using experimental point spread functions

Yiming Li[1], Markus Mund[1], Philipp Hoess[1], Joran Deschamps[1], Ulf Matti[1], Bianca Nijmeijer[1], Vilma Jimenez Sabinina[1], Jan Ellenberg[1], Ingmar Schoen[2] & Jonas Ries[1]

We present a real-time fitter for 3D single-molecule localization microscopy using experimental point spread functions (PSFs) that achieves minimal uncertainty in 3D on any microscope and is compatible with any PSF engineering approach. We used this method to image cellular structures and attained unprecedented image quality for astigmatic PSFs. The fitter compensates for most optical aberrations and makes accurate 3D super-resolution microscopy broadly accessible, even on standard microscopes without dedicated 3D optics.

As most biological structures have a 3D organization, it is desirable to achieve not only high lateral but also high axial resolution in super-resolution microscopy. Several methods have been developed to extend single-molecule localization microscopy (SMLM) to 3D applications. Most commonly, the *z*-position of a molecule is extracted from the shape of an astigmatic PSF[1]. Other approaches use more complex engineered PSFs (double-helix[2], phase-ramp[3], or tetrapod[4]) or a bi-plane configuration[5]. The vast majority of such 3D SMLM data is analyzed by fitting of a Gaussian PSF model, for the sake of computational simplicity[6]. However, real PSFs are poorly approximated by a Gaussian function (**Supplementary Fig. 1**), and they often show aberrations due to imperfect microscope optics. As a result, current 3D fitting routines do not reach the optimal 3D resolution, produce distortions, and are limited to a thin slice around the focal plane. Thus, they cannot realize the full potential of 3D SMLM for biological discovery.

As an alternative to simple Gaussian PSF models, fitting methods that use experimentally acquired PSFs have been developed that can in theory achieve greater precision, such as PSF correlation[7], phase retrieval[8,9], and interpolated PSFs[3,10–13]. In practice, however, these methods still have some limitations: they are too slow for online fitting during data acquisition; lack camera-specific noise models, which limits the use of scientific complementary metal-oxide semiconductor (sCMOS) cameras; and necessitate a challenging process to generate an accurate PSF model[14]. Additionally, nonintuitive interfaces, restrictive licenses, and dependencies on specific programming languages and libraries fundamentally complicate their use. Thus, simple Gaussian PSFs, and not experimental PSF models, are still generally used in 3D SMLM. For the majority of labs that have microscopes without perfect optics, this leads to much lower resolution in *z* than in *x* and *y*.

Here we present software that overcomes these limitations and makes experimental PSF fitting generally accessible and practically usable (**Supplementary Software 1** and **2**). It enables 3D SMLM on any microscope with optimal *z*-resolution by achieving the highest possible localization precision, the Cramér–Rao lower bound, as demonstrated on both simulated (**Supplementary Fig. 2**) and experimental (**Supplementary Fig. 3**) data. It contains a tool for calibrating the experimental PSF and a fitter for cubic spline (cspline) interpolated PSF models that reaches the necessary fitting speeds for real-time localization (>10^5 fits per second).

With this new software, we were able to resolve fine structural details of biological structures (**Fig. 1**, **Supplementary Fig. 4**) that were previously visible only with complex interferometric microscopes (**Supplementary Fig. 5**). For example, we resolved in 3D the hollow cylinders of immunolabeled microtubules with both DNA-PAINT (DNA-based point accumulation for imaging in nanoscale topography)[15] (**Fig. 1a**,**b**) and dSTORM (direct stochastic optical reconstruction microscopy)[16] (**Supplementary Fig. 6**) by using the simple astigmatic 3D method. Compared with the commonly used Gaussian fit[17], our fitter achieved higher precision and avoided distortions (**Fig. 1b**,**c**). We were able to visualize the spherical geometry of clathrin-coated pits without distortions and found that almost all localizations were in the clathrin coat, which highlights the high localization accuracy (**Fig. 1d**).

We achieved this performance by means of a systematic optimization in which we overcame bottlenecks encountered previously during fitting with experimental PSFs. First, we optimized the precision by developing a robust implementation of maximum-likelihood estimation (MLE) for spline-interpolated PSF models (**Supplementary Fig. 7**). Compared with simple Gaussian PSF models, our fitter reached substantially higher localization accuracies on both simulated (**Supplementary Fig. 8**) and experimental (**Supplementary Fig. 9**, **Fig. 1b**,**c**) data. Moreover, our fitter avoids the systematic error of Gaussian PSF models in estimating the number of photons per localization[18] (**Supplementary Fig. 10**). We note that use of a high-quality PSF model is vital to avoid

[1]Cell Biology and Biophysics Unit, European Molecular Biology Laboratory (EMBL), Heidelberg, Germany. [2]Molecular and Cellular Therapeutics, Royal College of Surgeons in Ireland, Dublin, Ireland. Correspondence should be addressed to J.R. (jonas.ries@embl.de).

RECEIVED 28 AUGUST 2017; ACCEPTED 6 MARCH 2018; PUBLISHED ONLINE 9 APRIL 2018; DOI:10.1038/NMETH.4661

artifacts commonly observed when experimental PSFs are used (**Supplementary Fig. 11**). To avoid these artifacts, we developed a simple tool to robustly create accurate experimental PSF models from several bead stacks (**Supplementary Software 1** and **2**).

Second, we optimized the speed of our fitter (**Fig. 1e**, **Supplementary Fig. 12**). High speeds are essential to allow fitting during data acquisition. This enables one to monitor the image quality in real time, and stop acquisitions as soon as a sufficient number of molecules have been localized[19] or if the sample is deemed unsatisfactory. By implementing our fitter on the graphical processing unit (GPU), we obtained fitting speeds more than 100 times faster than those of the fastest previously available implementation[13]. This allows online analysis, even of dense structures and large fields of view (**Fig. 1e**).

Third, we extended our fitter to sCMOS cameras (**Fig. 1e**), which offer fast imaging speeds and large fields of view, and thus are exquisitely suitable for SMLM[20]. For this, we included an sCMOS-specific noise model that was previously limited to simple Gaussian PSF models[20] in our fitter for experimental PSFs. We then verified that our fitter avoids camera noise-induced localization errors (**Supplementary Fig. 13**) and is fast enough for online analysis for sCMOS cameras (**Fig. 1e**).

Taken together, our results show that this software retains the ease of use and accessibility of astigmatic 3D SMLM while approaching a 3D image quality that has so far been achieved only with complex 4Pi microscopes[21].

However, astigmatism, like any other PSF engineering approach, requires dedicated 3D optics. Many users do not have access to such microscopes and are therefore limited to the acquisition of 2D data. Even unmodified PSFs contain information on the *z*-position of the fluorophore[22], which can be estimated from the PSF size or via the recently published photometry approach[18]. However, the *z*-resolution and axial range remain limited, and these methods cannot distinguish fluorophores above and below the focus because of the high symmetry of the PSF.

Here we overcame these limitations and extracted accurate and precise *z*-positions by fitting 2D SMLM data with an experimental model of the unmodified PSF. This allowed us to exploit subtle differences between the upper and lower halves of the PSF to correctly localize the fluorophore. To this end, we developed a bidirectional fitting approach in which we fit once with a starting *z*-parameter above the focus and a second time below the focus, and then choose the solution with the maximum likelihood.

We achieved a *z*-resolution almost as good as that of astigmatic PSFs (**Fig. 2a**,**b**, **Supplementary Figs. 4**, **8**, and **14**). We then directly compared our approach with existing methods based on PSF size (**Fig. 2c**) or photometry (TRABI)[18] (**Fig. 2d**). We found that only our software could resolve the nucleoplasmic and cytoplasmic rings of the nuclear pore complex, which are axially spaced by 53 nm (ref. 23). Although the *z*-resolution was slightly decreased close to the focal plane and 5% of misassignments led to a faint mirror image (**Fig. 2b**), our fitter enabled high-resolution 3D imaging directly on standard microscopes without any 3D optics.

Besides astigmatism, a variety of sophisticated PSF engineering approaches have been developed (double-helix[2], self-bending[24], tetrapod[4], phase-ramp[3], etc.) that increase the depth of field beyond ~1 µm but require complex data analysis. As our fitter is directly applicable to all these PSFs (**Supplementary Fig. 14**), it will allow many more labs to exploit the advantages of advanced PSF engineering for large sample volumes. Moreover, it allows the use of advanced PSF engineering with sCMOS cameras while accurately accounting for the camera noise.

To summarize, we have presented a fast and precise single-molecule fitter for arbitrary PSF models. This allowed us to achieve substantially improved 3D resolution and image quality with engineered astigmatic PSFs or unmodified PSFs from a standard microscope. Because deformations of the PSF are included in the experimental PSF model, our fitter is robust with respect to field-independent aberrations, and thus provides high accuracy even with objectives with a mediocre PSF or imperfect alignment of the microscope (**Supplementary Figs. 14** and **15**). The

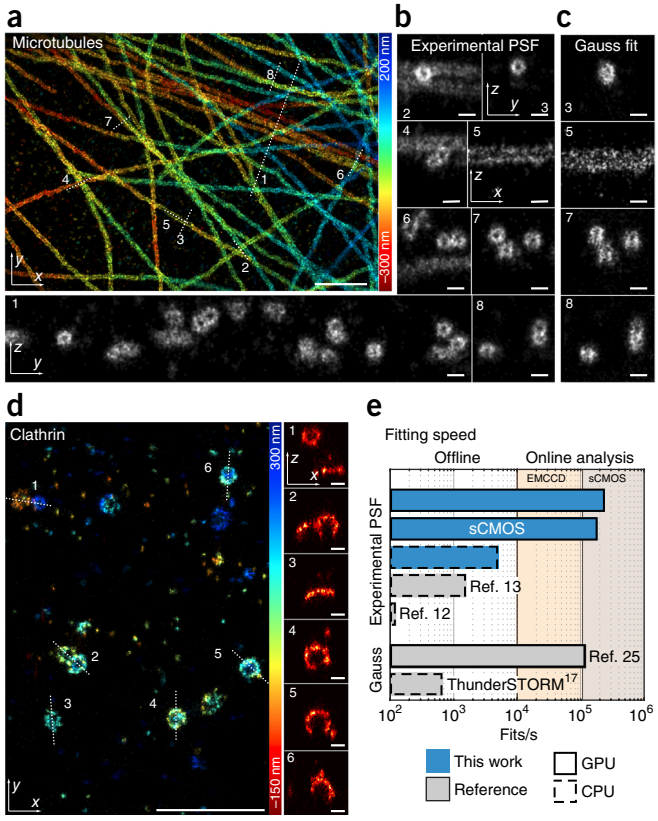

Figure 1 | Reconstruction of cellular structures with high 3D resolution using the real-time fitter for experimental PSFs. (**a**) Immunolabeled microtubules imaged with DNA-PAINT[15]. Localizations are color-coded according to their *z*-position. Corresponding localization precisions and profiles are shown in **Supplementary Figure 4**. Numbers 1–8 correspond to magnified views in **b** and **c**. (**b**) Side-view cross-sections along the lines shown in **a**. (**c**) Side-view reconstructions of the same areas shown in **b**, analyzed with ThunderSTORM[17] using an elliptical Gaussian MLE fit. (**d**) Immunolabeled clathrin imaged with dSTORM[16]. The images on the right are side-view cross-sections along the lines numbered in the left-hand image. (**e**) Fitting speed of the fitter presented in this work compared with those of previous implementations of fitters for experimental PSF models[12,13] and Gaussian PSF models[17,25]. Fits per second were measured on an i7-5930 CPU and a GTX1070 consumer graphics card. EMCCD, electron-multiplying charge-coupled device. Widths of the cross-sections were as follows: 150 nm (**b** (1, 4, 6)), 200 nm (**b** (2, 3, 7, 8)), 30 nm (**b** (5)), or 50 nm (**d**). Scale bars, 1 µm (**a**,**d**) or 100 nm (**b**,**c**, *x*–*z* reconstructions in **d**). All data and images in this figure are representative of ≥3 experiments.

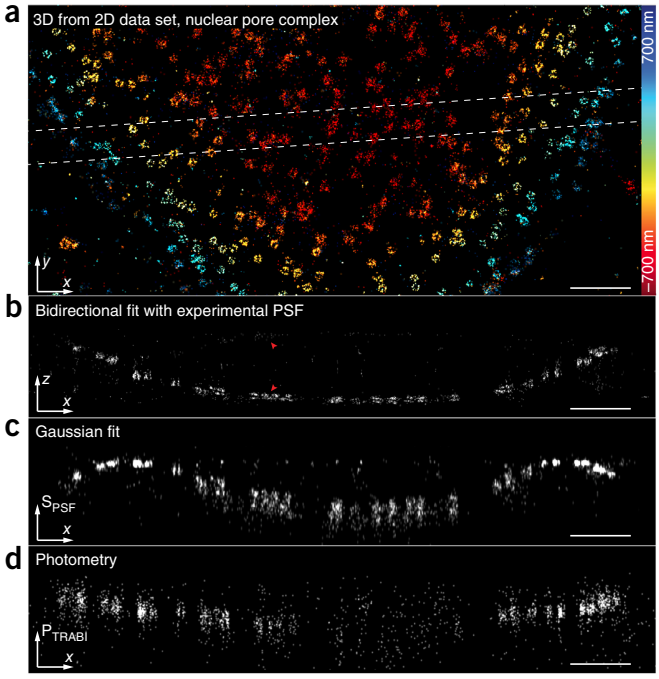

Figure 2 | Accurate 3D positions from a 2D data set with an unmodified PSF. (**a**) Nup107–SNAP–Alexa Fluor 647 imaged with dSTORM on a standard microscope without 3D optics. (**b**) Side-view reconstruction of the region bounded by dashed lines in **a**. The red arrowheads indicate nuclear pore complexes and their mirror images caused by misassignments. (**c**) Side-view reconstruction of the same region as in **b**, using the size of the PSF (S_{PSF}) from a fit with a symmetric Gaussian PSF model as a measure for the *z*-position. (**d**) Side-view reconstruction of the same region as in **b** and **c**, using the photometry-based intensity ratio[18] P_{TRABI} as a measure for the *z*-position. Corresponding localization precisions and profiles can be found in **Supplementary Figure 4**. Scale bars, 1 µm. All data and images in this figure are representative of ≥5 experiments.

presented framework is not restricted to bead-stack-based PSFs, but can be used in the same way to obtain and rapidly fit a spline interpolation of an arbitrary analytical or phase-retrieved PSF model, for which aberrations can be calculated and added computationally.

To enable the community to profit from these innovations, we developed easy-to-use fitting software and provide our CPU-based C code and the GPU-based CUDA code as open-source files (**Supplementary Software 1** and **2**; also available at https://github.com/jries/fit3Dcspline.git). The software can be incorporated in any programming language, as it is not library dependent, and should improve the speed and accuracy of any existing single-molecule fitting software.

We hope that our software will transform 3D SMLM from an experts-only technique into a broadly accessible high-resolution imaging methodology.

METHODS

Methods, including statements of data availability and any associated accession codes and references, are available in the online version of the paper.

Note: Any Supplementary Information and Source Data files are available in the online version of the paper.

ACKNOWLEDGMENTS

We thank J. Mehl for helping with the sample preparation and data acquisition, S. van der Linde (University of Glasgow) for help with the TRABI analysis, E. Klotzsch (University of New South Wales) for the Zeiss Elyra bead stacks, M. Lampe (ALMF, EMBL Heidelberg) for help with the acquisition on the Leica GSD, system and D. Drubin (University of California, Berkeley, Berkeley, California, USA) for the gift of SK-MEL-2 hCLTA(EN)/DNM2(EN) cells. This work was supported by the European Research Council (ERC CoG-724489 to M.M. and J.R.), the Deutsche Forschungs Gemeinschaft (DFG RI 2380/2 to J.R. and J.D.), the EMBL Interdisciplinary Postdoc Programme (EIPOD) under Marie Curie Actions COFUND (Y.L.), the 4D Nucleome/4DN NIH Common Fund (U01 EB021223 to J.E. and J.R.), and the European Molecular Biology Laboratory (Y.L., M.M., P.H., J.D., U.M., B.N., V.J.S., J.E., and J.R.).

AUTHOR CONTRIBUTIONS

Y.L. and J.R. conceived the approach, developed the methods, wrote the software, and analyzed the data. M.M. imaged clathrin-coated pits. P.H. imaged nuclear pore complexes. U.M. carried out DNA-PAINT imaging of microtubules. B.N., V.J.S., and J.E. contributed the Nup107 cell line. I.S. contributed the custom-made DNA-PAINT antibodies. J.D. acquired the aberrated PSFs and helped with the data analysis. Y.L., M.M., and J.R. wrote the manuscript with input from all other authors.

COMPETING INTERESTS

The authors declare no competing interests.

1. Huang, B., Wang, W., Bates, M. & Zhuang, X. *Science* **319**, 810–813 (2008).
2. Pavani, S.R.P. *et al. Proc. Natl. Acad. Sci. USA* **106**, 2995–2999 (2009).
3. Baddeley, D., Cannell, M.B. & Soeller, C. *Nano Res.* **4**, 589–598 (2011).
4. Shechtman, Y., Sahl, S.J., Backer, A.S. & Moerner, W.E. *Phys. Rev. Lett.* **113**, 133902 (2014).
5. Juette, M.F. *et al. Nat. Methods* **5**, 527–529 (2008).
6. Deschout, H. *et al. Nat. Methods* **11**, 253–266 (2014).
7. York, A.G., Ghitani, A., Vaziri, A., Davidson, M.W. & Shroff, H. *Nat. Methods* **8**, 327–333 (2011).
8. Quirin, S., Pavani, S.R.P. & Piestun, R. *Proc. Natl. Acad. Sci. USA* **109**, 675–679 (2012).
9. Liu, S., Kromann, E.B., Krueger, W.D., Bewersdorf, J. & Lidke, K.A. *Opt. Express* **21**, 29462–29487 (2013).
10. Tahmasbi, A., Ward, E.S. & Ober, R.J. *Opt. Express* **23**, 7630–7652 (2015).
11. Mlodzianoski, M.J., Juette, M.F., Beane, G.L. & Bewersdorf, J. *Opt. Express* **17**, 8264–8277 (2009).
12. Kirshner, H., Vonesch, C. & Unser, M. in *2013 IEEE 10th International Symposium on Biomedical Imaging* 588–591 (IEEE, 2013).
13. Babcock, H.P. & Zhuang, X. *Sci. Rep.* **7**, 552 (2017).
14. Deng, Y. & Shaevitz, J.W. *Appl. Opt.* **48**, 1886–1890 (2009).
15. Schnitzbauer, J., Strauss, M.T., Schlichthaerle, T., Schueder, F. & Jungmann, R. *Nat. Protoc.* **12**, 1198–1228 (2017).
16. van de Linde, S. *et al. Nat. Protoc.* **6**, 991–1009 (2011).
17. Ovesný, M., Křížek, P., Borkovec, J., Švindrych, Z. & Hagen, G.M. *Bioinformatics* **30**, 2389–2390 (2014).
18. Franke, C., Sauer, M. & van de Linde, S. *Nat. Methods* **14**, 41–44 (2017).
19. Nieuwenhuizen, R.P.J. *et al. Nat. Methods* **10**, 557–562 (2013).
20. Huang, F. *et al. Nat. Methods* **10**, 653–658 (2013).
21. Huang, F. *et al. Cell* **166**, 1028–1040 (2016).
22. Aguet, F., Van De Ville, D. & Unser, M. *Opt. Express* **13**, 10503–10522 (2005).
23. von Appen, A. *et al. Nature* **526**, 140–143 (2015).
24. Jia, S., Vaughan, J.C. & Zhuang, X. *Nat. Photonics* **8**, 302–306 (2014).
25. Smith, C.S., Joseph, N., Rieger, B. & Lidke, K.A. *Nat. Methods* **7**, 373–375 (2010).

ONLINE METHODS

Robust averaging of experimental bead stacks. Stacks of beads, immobilized on a coverslip, were acquired in a range of ±1,000 nm with respect to the coverslip. A spacing in z between 10 nm and 50 nm works well. Beads in each stack were segmented in a maximum-intensity projected image by maximum finding and thresholding. Sub-regions around each bead location were cropped. Next, we aligned all beads with sub-pixel accuracy by 3D cross-correlation using a single bead as a reference. To gain precision, we carried out another round of 3D alignment of the central part of each stack, using the average of the aligned bead stacks as the reference. We scaled up the central part of the cross-correlation by a factor of 20 by cspline interpolation and determined the x, y, and z shifts from the position of the maximum[26]. The bead stacks were shifted by means of cspline interpolation. Iteratively, bead stacks that showed substantial dissimilarity to the average were identified on the basis of the maximum value of the cross-correlation and the mean square error and were excluded from the average. To eliminate the background, we subtracted the minimum value of the bead stack and normalized the amplitude by the total (summed) intensity of the central slice. We further regularized the bead stack by smoothing it in the z-direction with a smoothing B-spline[27]. In the presence of field-dependent aberrations, systematic fitting errors can be corrected in a post-processing step based on a precise calibration[28]. We suggest that in the presence of strong field-dependent aberrations, users perform the calibration and fitting only locally on small sub-regions of near-uniform aberrations.

Calculation of cspline-interpolated PSFs. Spline functions are piecewise polynomials for which high-order derivatives are continuous at the knots, where the pieces connect. Cubic splines are the most commonly used splines, for example, in computer graphics, geometric modeling, and so on. Recently, this type of approximation theory has also been used for single-molecule localization[10,12,13]. We implemented the cspline interpolation in terms of both csplines and cubic B-splines. A B-spline interpolation is generally less memory intensive because only one B-spline coefficient is needed in each spline interval. In comparison, $(d+1)^n$ coefficients are required in each spline interval for spline polynomials, where d is the spline degree and n is the dimension. However, our implementation of a 3D fit based on csplines is about 2.5 times faster than the cubic B-spline form because csplines are more explicit and fewer calculations are needed to calculate spline values and derivatives. Therefore, the software used in this work is based on csplines with 64 coefficients in each voxel of the 3D PSF stack.

Similar to ref. 13, the 3D PSF is described by a 3D cspline for voxel (i, j, k) as follows:

$$f_{i,j,k}(x,y,z) = \sum_{m=0}^{3}\sum_{n=0}^{3}\sum_{p=0}^{3} a_{i,j,k,m,n,p} \left(\frac{x-x_i}{\Delta x}\right)^m \left(\frac{y-y_j}{\Delta y}\right)^n \left(\frac{z-z_k}{\Delta z}\right)^p$$

where Δx and Δy are the pixel size of the PSF in the object space in the x and y directions, respectively; Δz is the step size in the objective space in the z direction; and x_i, x_j, and z_k are the start positions of voxel (i, j, k) in the x, y, and z directions, respectively.

To calculate the cspline coefficients, we first built the 3D PSF stack by averaging the bead stacks from different fields of view by 3D cross-correlation and by regularization, as described above. The spline coefficients were built on the basis of the averaged and smoothed 3D PSF stack. As 64 cspline coefficients are required to describe each voxel, we upsampled (cspline interpolation) each voxel three times in the x, y, and z directions, respectively. The 64 upsampled coordinates (including the boundary of neighboring voxels) were used to calculate the 64 cspline coefficients. The code to calculate the spline coefficients from bead stacks can be found in **Supplementary Software 1**.

***z*-calibration of astigmatic Gaussian PSF models.** Our PSF calibration tool also allows the user to extract z-positions by using two widely used algorithms: (A) calculation of the z-positions directly from the calibrated $\sigma_x(z)$ and $\sigma_y(z)$ returned by the elliptical Gaussian fit; and (B) determination of the z-positions by direct fitting of single molecules with the calibrated astigmatic Gaussian PSF model[29].

For both calibrations, the bead stacks are fitted with an elliptical Gaussian PSF model and shifted in z according to their true z-positions where $\sigma_x(z) = \sigma_y(z)$. The outliers are removed on the basis of the root mean error of $\sigma_x(z)$ and $\sigma_y(z)$ with respect to the average curves.

For algorithm A, we calculate $d\sigma^2(z) = \sigma_x(z)^2 - \sigma_y(z)^2$ and interpolate the functional relationship $z(d\sigma^2)$ by a smoothing cubic B-spline. This B-spline interpolation is then used to directly read out z from $d\sigma^2$.

For algorithm B, $\sigma_x(z)$ and $\sigma_y(z)$ are fitted with a polynomial approximation for the astigmatic Gaussian model:

$$\sigma_x(z) = \sigma_{0x}\sqrt{1+\left(\frac{z-\gamma}{d}\right)^2 + A_x\left(\frac{z-\gamma}{d}\right)^3 + B_x\left(\frac{z-\gamma}{d}\right)^4}$$

$$\sigma_y(z) = \sigma_{0y}\sqrt{1+\left(\frac{z-\gamma}{d}\right)^2 + A_y\left(\frac{z-\gamma}{d}\right)^3 + B_y\left(\frac{z-\gamma}{d}\right)^4}$$

The parameters σ_{0x}, A_x, B_x, σ_{0y}, A_y, B_y, γ, and d are input parameters for the Gaussian fitter, which directly returns the z-coordinates of the fluorophores. We followed the formula in ref. 25 to calculate the derivatives of the parameters. However, the iterative process was reimplemented using the Levenberg–Marquardt (L-M) algorithm.

Newton and Levenberg–Marquardt iterative schemes for MLE. MLE is the method of choice for fitting data with Poisson statistics[30]. The objective function for MLE is given by[31]

$$\chi^2_{\mathrm{MLE}} = 2\left(\sum_k (\mu_k - x_k) - \sum_{k,x_k>0} x_k \ln(\mu_k / x_k)\right)$$

where μ_k is the expected number of photons in pixel k from the model PSF function, and x_k is the measured number of photons. By minimizing χ^2_{MLE}, one obtains the maximum likelihood for the Poisson process.

Methods for nonlinear optimization are usually iterative. For Newton iterative schemes, the search direction $\Delta\theta_i$ of each iteration is given by[25]

$$\frac{\partial^2 \chi^2_{\mathrm{MLE}}}{\partial \theta_i^2}\Delta\theta_i = -\frac{\partial \chi^2_{\mathrm{MLE}}}{\partial \theta_i}$$

where θ_i is the ith free fit parameter. However, computation of the second derivatives is often quite difficult and can be destabilizing when the model fits badly or is contaminated by outlier points[30].

An alternative method is the L-M algorithm. The L-M algorithm is often used for least-squares fitting because it is quick and robust. With relatively simple modifications[31], the L-M algorithm has also been used to minimize χ^2_{MLE}. In the L-M algorithm, the second-derivatives term is neglected and only the first derivatives are used. In the L-M algorithm, the update $\Delta\theta_i$ is given by

$$\left(H_{i,j} + \lambda I\right)\Delta\theta_i = J_j$$

where $H_{i,j}$ is the Hessian matrix without the second partial derivatives term, defined as

$$H_{i,j} = \sum_k \frac{\partial \mu_k}{\partial \theta_i}\frac{\partial \mu_k}{\partial \theta_j}\frac{x_k}{{\mu_k}^2}$$

J_j is the Jacobian matrix, defined as

$$J_j = \sum_k \frac{\partial \mu_k}{\partial \theta_j}\frac{(x_k - \mu_k)}{\mu_k}$$

λ is the damping factor, and I is a diagonal matrix equal to the diagonal elements of the Hessian matrix. This method is more robust because a damping factor is introduced and the second derivatives do not contribute. This damping factor is increased (multiplied by 10 in this work) if an iteration step does not decrease χ^2_{MLE} or $H_{i,j}$ is not positive definite.

GPU implementation. This GPU implementation of the iterative method follows the framework developed for fitting a Gaussian PSF model using a GPU[25], but using the L-M algorithm. We note that a general framework for L-M fitting on a GPU was published recently[32]. Unlike previous work for electron-multiplying charge-coupled device (EMCCD) and sCMOS noise models[20,25] in which the shared memory was used to store the molecule-candidate data and readout noise map, we kept the data in the GPU global memory. Each thread is pointed to each molecule candidate and performs all the computations for each molecule candidate. No thread synchronization is required. We used 64 threads per block. The overall speed is about 1.9 times (small window size) to 47.9 times (large window size) faster (**Supplementary Fig. 12**) than for the original code where shared memory was used for the sCMOS noise model. We assume that this is due to the compiler optimization where more registers are used and the time for copying data from the global to the shared memory is saved. Both the CPU-based C code and the GPU-based CUDA code were compiled in Microsoft Visual Studio 2010. The software was called via Matlab (Mathworks) MEX files. It was run on a personal computer using an Intel Core i7-5930 processor clocked at 3.50 GHz with 64 GB memory. An NVIDIA GeForce GTX 1070 graphics card with 8.0 GB memory was used for GPU-based computation.

Simulation of realistic single-molecule data. To simulate single-molecule images using a realistic PSF model, we used the cspline-interpolated PSF model generated from experimental bead stacks as described above. We generated the single-molecule image from this PSF model at a random 3D position, multiplied it by the number of photons per localization, and added a constant background. Finally, we applied Poisson noise to the images. For simulations of sCMOS data, we added pixel-dependent Gaussian noise. The code to simulate PSFs from the calculated cspline coefficients can be found in **Supplementary Software 1**.

MLE fit using an sCMOS camera noise model. sCMOS cameras have become more and more attractive for localization microscopy owing to their fast data acquisition even for large fields of view, low readout noise, and relatively low price. However, their intrinsic pixel-dependent gain, offset, and readout noise can create a localization bias, which has to be corrected for localization of a single molecule[20]. Gain g_k and offset o_k in pixel k can be taken into account when the camera image I_k^{ADU} in analog digital units (ADU) is converted into photons:

$$I_k^P = \frac{I_k^{\mathrm{ADU}} - o_k}{g_k}$$

The readout noise, however, has to be taken into account during the fitting in the noise model and can be calculated from many dark camera images as the pixel-wise variance. Here we use the model proposed by Huang *et al.*[20], which approximates the normal distributed readout noise (var_k, in units of photoelectrons) with a Poisson distribution. When the pixel-dependent constant var_k is added to the measured photoelectrons, one can expect the new value to approximate a Poisson distribution with a mean of $\mu_k + \mathrm{var}_k$. Here, μ_k is the expected photon number in pixel k of the PSF model function. Therefore, in comparison to the conventional MLE fit for EMCCD data, only one more parameter, var_k, is required for sCMOS data. Also, var_k is only kept in the global memory of the GPU. Compared with the EMCCD noise model, the speed of the algorithm was reduced by only <25% because of its accounting for the pixel-dependent readout noise (**Supplementary Fig. 12**).

3D fitting of SMLM data acquired with standard microscopes without 3D optics. Because our code includes fitting with arbitrary PSFs, it is directly applicable to 2D data acquired with an unmodified PSF in a standard microscope. A model for the unmodified PSF can be calculated directly from bead stacks, analogously to engineered PSFs. However, the unmodified PSF has high symmetry with respect to the focal plane (**Supplementary Fig. 1**), which makes it difficult for an iterative fitting procedure to converge through the focal plane. To overcome this problem, we fit every localization twice: once with a starting parameter for the z-position 500 nm above the focal plane, and once with a starting parameter 500 nm below the focal plane. The maximum likelihood is then used to select the better fit. Because a real PSF is not completely symmetrical[33], this breaks the degeneracy previously encountered with extraction of z-positions in 2D data sets from only a single photometry or PSF size parameter[18].

Owing to the rather large size of the calibration bead (100 nm) and small inaccuracies during the averaging of many bead stacks,

doi:10.1038/nmeth.4661

the cspline PSF model is slightly blurred compared with a single-molecule PSF. This had no apparent effect on 3D data, but in 2D data it led to an accumulation of fitted localizations at the focal plane. To overcome this problem, we filtered the raw images with a Gaussian kernel (s.d. $\sigma < 0.5$ pixels), thus applying the blur in the PSF model to the data. To find the right value of σ, we fitted a subset of the data with several values for σ (0, 0.1, …, 0.5) and selected the σ value for which we found neither an accumulation nor a depletion of localizations around the focal plane.

Post-processing. As the positions used above are all based on the objective positions, which differ from the true absolute positions owing to refractive index mismatch, we further multiply the *z*-positions by a refractive index mismatch factor of 0.75 (ref. 1). Then, *x*-, *y*-, and *z*-positions were corrected for residual drift by a custom algorithm based on redundant cross-correlation. Localizations persistent in consecutive frames were grouped into one localization, and super-resolution images were constructed with every localization rendered as a 2D elliptical Gaussian with a width proportional to the localization precision.

For measurements deep in the sample obtained with oil-immersion objectives, aberrations induced by the refractive index mismatch can be corrected for as described in ref. 34.

Sample preparation of clathrin-coated pits in SK-MEL-2 cells. All samples were imaged on round 24-mm high-precision glass coverslips (No. 1.5H; 117640; Marienfeld, Lauda-Königshofen, Germany). Coverslips were cleaned overnight in a 1:1 mixture of concentrated HCl and methanol, rinsed with Millipore water until neutral, dried, and UV-sterilized in a standard cell-culture hood.

SK-MEL-2 cells (a kind gift from David Drubin, UC Berkeley; described in ref. 35) were cultured under adherent conditions in DMEM/F12 (Dulbecco's modified Eagle's medium combined with Nutrient Mixture F-12) with GlutaMAX and phenol red (Thermo Fisher; 10565018) supplemented with 10% (v/v) FBS, ZellShield (Biochrom AG, Berlin, Germany), and 30 mM HEPES at 37 °C, 5% CO_2, 100% humidity. Cells were fixed using 3% (w/v) formaldehyde (FA) in cytoskeleton buffer (CB; 10 mM MES, pH 6.1, 150 mM NaCl, 5 mM EGTA, 5 mM D-glucose, 5 mM $MgCl_2$; described in ref. 36) for 20 min. Fixation was stopped by incubation in 0.1% (w/v) $NaBH_4$ for 7 min. The sample was washed with PBS three times and subsequently permeabilized with 0.01% (w/v) digitonin (Sigma-Aldrich, St. Louis, MO, USA) in PBS for 15 min. After being washed twice with PBS, the sample was blocked with 2% (w/v) BSA in PBS for 60 min, washed again with PBS, and stained for 3–12 h with anti-clathrin light chain (sc-28276; Santa Cruz Biotechnology, Dallas, TX, USA; diluted 1:300) and anti-clathrin heavy chain rabbit polyclonal antibodies (ab21679; Abcam, Cambridge, UK; diluted 1:500) in 1% (w/v) BSA in PBS. The sample was washed with PBS three times and then incubated with a donkey anti-rabbit secondary antibody (711-005-152; Jackson ImmunoResearch, West Grove, PA, USA) conjugated to Alexa Fluor 647–NHS at an average degree of labeling of 1.5 for 4 h. Finally, the sample was washed three times with PBS prior to imaging.

For dSTORM imaging, coverslips were mounted in 500 µL of blinking buffer (50 mM Tris, pH 8, 10 mM NaCl, 10% (w/v) D-glucose, 35 mM 2-mercaptoethylamine, 500 µg/mL GLOX, 40 µg/mL catalase, 2 mM COT).

Sample preparation for imaging of the nuclear pore complex and microtubules. Wild-type U-2 OS and genome-edited U-2 OS cells that expressed Nup107–SNAP[37] were cultured under adherent conditions in DMEM (high-glucose, without phenol red) supplemented with 10% (v/v) FBS, 2 mM L-glutamine, non-essential amino acids, and ZellShield at 37 °C, 5% CO_2, 100% humidity. All incubations were carried out at room temperature. For nuclear pore staining, the coverslips were rinsed twice with PBS and prefixed with 2.4% (w/v) FA in PBS for 30 s. Cells were permeabilized with 0.4% (v/v) Triton X-100 in PBS for 3 min and then fixed with 2.4% (w/v) FA in PBS for 30 min. Subsequently, the fixation reaction was quenched by incubation in 100 mM NH_4Cl in PBS for 5 min. After being washed twice with PBS, the samples were blocked with Image-iT FX signal enhancer (Thermo Fisher Scientific, Waltham, MA, USA) for 30 min. The coverslips were incubated in staining solution (1 µM benzylguanine Alexa Fluor 647 (S9136S; NEB, Ipswich, MA, USA), 1 mM DTT, 1% (w/v) BSA in PBS) for 50 min in the dark. After being rinsed three times with PBS and washed three times with PBS for 5 min, the sample was mounted for imaging.

For microtubule staining, wild-type U-2 OS cells were prefixed for 2 min with 0.3% (v/v) glutaraldehyde in CB + 0.25% (v/v) Triton X-100 and fixed with 2% (v/v) glutaraldehyde in CB for 10 min. Fluorescent background was reduced by incubation with 0.1% (w/v) $NaBH_4$ in PBS for 7 min. After samples had been washed three times with PBS, microtubules were stained with anti-α-tubulin (MS581; NeoMarkers, Fremont, CA, USA) 1:300 in PBS + 2% (w/v) BSA for 2 h and anti-mouse Alexa Fluor 647 (A21236; Invitrogen, Carlsbad, CA, USA) 1:300 in PBS + 2% (w/v) BSA for 2 h. After being washed three times with PBS, samples were imaged in blinking buffer as described above, but with pyranose oxidase instead of glucose oxidase.

For DNA-PAINT imaging, microtubules were labeled with anti-α-tubulin (MS581, NeoMarkers, and T6074; Sigma-Aldrich, St. Louis, MO, USA) and anti-β-tubulin (T5293; Sigma-Aldrich), each diluted 1:300 in PBS with 2% (w/v) BSA, for 2 h. After being washed three times with PBS, samples were incubated with a DNA-labeled anti-mouse secondary antibody overnight (docking strand sequence: 5′-TTATACATCTA-3′) and imaged after 5 washes with PBS using 50 pM of complementary Atto-655-labeled DNA imager strand (5′-CTAGATGTAT-3′-Atto655) in PAINT buffer (PBS, 500 mM NaCl, 40 mM Tris, pH 8.0).

Microscopy. SMLM image acquisition was performed at room temperature (24 °C) on a customized microscope[38] equipped with a high-numerical-aperture (NA) oil-immersion objective (160×/1.43-NA; Leica, Wetzlar, Germany). We used a laser combiner (LightHub; Omicron-Laserage Laserprodukte, Dudenhofen, Germany) with Luxx 405, 488, and 638 Cobolt 561 lasers. The lasers were triggered using a field-programmable gate array (Mojo; Embedded Micro, Denver, CO, USA), allowing microsecond pulsing control of lasers. After passing through a speckle reducer (LSR-3005-17S-VIS; Optotune, Dietikon, Switzerland), the laser is guided through a multimode fiber (M105L02S-A; Thorlabs, Newton, NJ, USA). The output of the fiber is first magnified by an achromatic lens and then imaged into the sample[38]. A laser clean-up filter (390/482/563/640 HC Quad; AHF, Tübingen, Germany) is placed in the beam path to remove fiber-generated fluorescence. A closed-loop focus lock system was implemented, using

the signal of a near-infrared laser reflected by the coverslip and its detection by a quadrant photodiode. The focus can be stabilized within ±10 nm over several hours[39]. The fluorescence emission was filtered by a bandpass filter (700/100, AHF or 676/37, AHF) and recorded by an EMCCD camera (Evolve512D; Photometrics, Tucson, AZ, USA). Typically, we acquire 100,000–300,000 frames with a 15-ms exposure time (100 ms for DNA-PAINT) and laser power densities of ~15 kW/cm^2. The pulse length of the 405-nm laser is automatically adjusted to retain a constant number of localizations per frame.

Controlled induction of optical aberrations was carried out on a similar microscope, albeit with an additional detection path. After the tube lens, the back focal plane of the objective is imaged onto a deformable mirror (Mirao 52e; Imagine Optic, Orsay, France) for phase correction. A flip mirror allows the light to be guided toward either a Shack–Hartmann wavefront sensor (HASO3; Imagine Optic) or the camera for fluorescence imaging. We obtained the PSFs by correcting the optical aberrations using a closed loop between the mirror and the wavefront sensor in Casao (Imagine Optic) and applying image-based optimization of a single bead in Micao (Imagine Optic). Aberrations were then induced on the basis of pure Zernike modes.

Furthermore, SMLM images were acquired on a commercial Leica SR GSD 3D microscope. The setup is equipped with a 500-mW 642-nm laser (MPBC Inc., Montreal, Quebec, Canada), a 30-mW 405-nm diode laser (Coherent Inc., Santa Clara, CA, USA), a DBP 405/10 642/10 excitation filter, an LP649 dichroic mirror, a BP 710/100 emission filter, and a high-NA oil-immersion objective (160×/1.43-NA; Leica). Astigmatism was induced with a modified tube lens, and the image was recorded on an iXon3 897 EMCCD camera (Andor, Belfast, Northern Ireland). Reference images were reconstructed with Leica Application Suite X (version 1.9.0.13747) and used for comparison to the cspline fit.

Statistics and reproducibility. Figures show representative data from ≥3 (**Fig. 1**, **Supplementary Figs. 6** and **11**) or ≥5 (**Fig. 2**, **Supplementary Fig. 1**) representative experiments, or from single experiments (**Supplementary Figs. 9**, **14**, and **15**). **Supplementary Figure 13** shows representative data from three similar independent simulations.

Code availability. Source code for the software used in this study is contained in **Supplementary Software 1**, and updated versions can be freely downloaded at https://github.com/jries/fit3Dcspline.git.

Life Sciences Reporting Summary. Further information on experimental design is available in the **Life Sciences Reporting Summary**.

Data availability. The data sets generated and analyzed in this study are available from the corresponding author upon reasonable request.

26. Guizar-Sicairos, M., Thurman, S.T. & Fienup, J.R. *Opt. Lett.* **33**, 156–158 (2008).
27. Unser, M., Aldroubi, A. & Eden, M. *IEEE Trans. Signal Process.* **41**, 821–833 (1993).
28. von Diezmann, A., Lee, M.Y., Lew, M.D. & Moerner, W.E. *Optica* **2**, 985–993 (2015).
29. Holtzer, L., Meckel, T. & Schmidt, T. *Appl. Phys. Lett.* **90**, 53902 (2007).
30. Press, W., Teukolsky, S., Vetterling, W. & Flannery, B. *Numerical Recipes in C: The Art of Scientific Computing* (Cambridge Univ. Press, Cambridge, UK, 1992).
31. Laurence, T.A. & Chromy, B.A. *Nat. Methods* **7**, 338–339 (2010).
32. Przybylski, A., Thiel, B., Keller-Findeisen, J., Stock, B. & Bates, M. *Sci. Rep.* **7**, 15722 (2017).
33. Kirshner, H., Aguet, F., Sage, D. & Unser, M. *J. Microsc.* **249**, 13–25 (2013).
34. Li, Y. *et al. bioRxiv* Preprint at https://www.biorxiv.org/content/early/2017/08/10/172643 (2017).
35. Doyon, J.B. *et al. Nat. Cell Biol.* **13**, 331–337 (2011).
36. Xu, K., Zhong, G. & Zhuang, X. *Science* **339**, 452–456 (2013).
37. Otsuka, S. *et al. eLife* **5**, 1–23 (2016).
38. Deschamps, J., Rowald, A. & Ries, J. *Opt. Express* **24**, 28080–28090 (2016).
39. Ries, J., Kaplan, C., Platonova, E., Eghlidi, H. & Ewers, H. *Nat. Methods* **9**, 582–584 (2012).

doi:10.1038/nmeth.4661

nature research

Corresponding author(s): Jonas Ries

Initial submission ☐ Revised version ☐ Final submission ☒

Life Sciences Reporting Summary

Nature Research wishes to improve the reproducibility of the work that we publish. This form is intended for publication with all accepted life science papers and provides structure for consistency and transparency in reporting. Every life science submission will use this form; some list items might not apply to an individual manuscript, but all fields must be completed for clarity.

For further information on the points included in this form, see Reporting Life Sciences Research. For further information on Nature Research policies, including our data availability policy, see Authors & Referees and the Editorial Policy Checklist.

Experimental design

1. Sample size

Describe how sample size was determined.

No hypothesis based experiment was performed. Therefore, the sample size was not predetermined. For all simulations, the data size was chosen large enough that statistical errors are minimal compared to the effect.

2. Data exclusions

Describe any data exclusions.

For calculation of RMS error for Newton method, single data points for which localization error is more than 10 pixels (<5%) were excluded.

3. Replication

Describe whether the experimental findings were reliably reproduced.

All code is open source to help with the reproducibility of computational analysis. Experimental findings were reproduced successfully.

4. Randomization

Describe how samples/organisms/participants were allocated into experimental groups.

Not relevant for this study as the work presents an image analysis software. Presented data is either illustrative or the result of simulations.

5. Blinding

Describe whether the investigators were blinded to group allocation during data collection and/or analysis.

Not relevant for this study as the work presents an image analysis software

Note: all studies involving animals and/or human research participants must disclose whether blinding and randomization were used.

6. Statistical parameters

For all figures and tables that use statistical methods, confirm that the following items are present in relevant figure legends (or in the Methods section if additional space is needed).

n/a	Confirmed
☒	☐ The exact sample size (*n*) for each experimental group/condition, given as a discrete number and unit of measurement (animals, litters, cultures, etc.)
☒	☐ A description of how samples were collected, noting whether measurements were taken from distinct samples or whether the same sample was measured repeatedly
☒	☐ A statement indicating how many times each experiment was replicated
☒	☐ The statistical test(s) used and whether they are one- or two-sided (note: only common tests should be described solely by name; more complex techniques should be described in the Methods section)
☒	☐ A description of any assumptions or corrections, such as an adjustment for multiple comparisons
☒	☐ The test results (e.g. *P* values) given as exact values whenever possible and with confidence intervals noted
☒	☐ A clear description of statistics including central tendency (e.g. median, mean) and variation (e.g. standard deviation, interquartile range)
☒	☐ Clearly defined error bars

See the web collection on statistics for biologists for further resources and guidance.

Nature Methods: doi:10.1038/nmeth.4661

Software

Policy information about availability of computer code

7. Software

Describe the software used to analyze the data in this study.	Matlab 2017a, Windows Visual Studio 2010, custom Matlab and CUDA code (as supplementary software and available on github), Leica Application Suite X (Version 1.9.0.137), Babcock software (0f05748 2017-09-14), Kirshner Software (http://bigwww.epfl.ch/kirshner/). ThunderSTORM(e85c565 2017-01-29), Smith Software (gaussmelv2)

For manuscripts utilizing custom algorithms or software that are central to the paper but not yet described in the published literature, software must be made available to editors and reviewers upon request. We strongly encourage code deposition in a community repository (e.g. GitHub). *Nature Methods* guidance for providing algorithms and software for publication provides further information on this topic.

Materials and reagents

Policy information about availability of materials

8. Materials availability

Indicate whether there are restrictions on availability of unique materials or if these materials are only available for distribution by a for-profit company.	all unique materials are readily available from the authors.

9. Antibodies

Describe the antibodies used and how they were validated for use in the system under study (i.e. assay and species).	anti-clathrin: Abcam ab21679, 1:500; Santa Cruz Biotechnology sc-28276, 1:300 anti-rabbit secondary: Jackson ImmunoResarch 711-005-152, 1:300 tubulin: NeoMarkers MS581, 1:300, Sigma-Aldrich T6074, 1:300, Sigma-Aldrich T5293, 1:300; anti-mouse secondary antibody for DNA-PAINT is a custom labeled antibody available upon request from Ingmar Schoen. All antibodies showed a very high specificity for immunloabeling in superresolution microscopy.

10. Eukaryotic cell lines

a. State the source of each eukaryotic cell line used.	SK-MEL-2, kind gift of David Drubin (Berkeley) U 2-OS: ATCC (U-2OS ATCC HTB-96)
b. Describe the method of cell line authentication used.	none of the cell lines have been authenticated
c. Report whether the cell lines were tested for mycoplasma contamination.	cell lines were tested for mycoplasma contamination
d. If any of the cell lines used are listed in the database of commonly misidentified cell lines maintained by ICLAC, provide a scientific rationale for their use.	no commonly misidentified cell lines were used

Animals and human research participants

Policy information about studies involving animals; when reporting animal research, follow the ARRIVE guidelines

11. Description of research animals

Provide details on animals and/or animal-derived materials used in the study.	no animals were used

Policy information about studies involving human research participants

12. Description of human research participants

Describe the covariate-relevant population characteristics of the human research participants.	the study did not involve human research participants

Nature Methods: doi:10.1038/nmeth.4661